Earth Planets Space, **54**, 45–56, 2002

Observations and modeling of 630 nm airglow and total electron content associated with traveling ionospheric disturbances over Shigaraki, Japan

T. Ogawa[1], N. Balan[1*], Y. Otsuka[1], K. Shiokawa[1], C. Ihara[1], T. Shimomai[1**], and A. Saito[2]

[1]*Solar-Terrestrial Environment Laboratory, Nagoya University, Toyokawa, Aichi 442-8507, Japan*
[2]*Department of Geophysics, Graduate School of Science, Kyoto University, Kyoto 606-8502, Japan*

(Received October 31, 2000; Revised April 13, 2001; Accepted April 13, 2001)

Southwestward-propagating medium-scale traveling ionospheric disturbances (MSTIDs) observed over Shigaraki (34.85°N, 136.10°E) in Japan on the night of May 22, 1998 are analyzed in detail. The MSTIDs were detected with a 630.0 nm (OI) all-sky imager at Shigaraki and a large number of GPS (Global Positioning System) receivers distributed around Shigaraki. Each GPS receiver provided total electron content (TEC) between the GPS altitude (20,200 km) and the ground. MSTID amplitudes varied in space and time, and showed decay and enhancement during the southwestward propagation, suggesting that amplitudes of atmospheric gravity waves and the interaction process between gravity waves and *F* region plasma were highly variable. It is found that spatial and temporal fluctuations of the 630 nm intensity are well correlated with those of GPS-TEC except for a certain period of time. The Scheffield University Plasmasphere Ionosphere Model (SUPIM) is used to obtain theoretical relationships between the 630 nm airglow intensity and GPS-TEC and between their fluctuation amplitudes. The results indicate that the fluctuation amplitudes observed in weak airglow regions are caused by an electron density fluctuation of about ±20% occurring around an altitude of 250 km, where the 630 nm emission rate reaches a maximum, below the *F* layer peak altitude. Highly enhanced 630 nm intensity and GPS-TEC within a bright airglow region are due to an electron density enhancement of about 150% occurring at altitudes below 300 km.

1. Introduction

Since Hines (1960) suggested the important role of atmospheric gravity waves in inducing large-scale wavy structures (say, ≥100 km) in the ionospheric plasma, traveling ionospheric disturbances (TIDs) in the *F* region, which are ionospheric manifestations of atmospheric gravity waves, have been extensively observed using radio techniques such as ionosonde, incoherent scatter radar, HF Doppler, satellite beacon wave reception, etc.; see reviews by Hunsucker (1982) and Hocke and Schlegel (1996). These techniques have disclosed various characteristics of TID structure and propagation although most of the observations have been made at a fixed location with a single method.

The recent advent of new observation techniques using all-sky CCD imagers and Global Positioning System (GPS) satellite signals has brought about new insights into the two-dimensional properties of TIDs. In particular, in Japan we have a network of 630.0 nm (OI) airglow imagers and an extremely dense GPS network (GEONET; GPS Earth Observation Network) consisting of about 1000 receivers capable of measuring total electron content (TEC) between the GPS altitude (20,200 km) and the ground. This network, covering the mid-latitudes around Japan, has been very useful for finding new features of two-dimensional TID characteristics over a very wide area (Saito *et al.*, 1998, 2001, 2002; Kubota *et al.*, 2000) that were never found in previous observations (e.g., Maeda and Handa, 1980; Shibata and Okuzawa, 1983; Ogawa *et al.*, 1994; Oliver *et al.*, 1995).

The first FRONT (*F* region Radio and Optical measurement of Nighttime TID) campaign to study TIDs over Japan and their physical processes was conducted in May 1998. On the night of May 22, clear medium-scale TIDs (MSTIDs) were observed with both the 630 nm all-sky imager network (Kubota *et al.*, 2000) and GEONET (Saito *et al.*, 2001). The spatial and temporal MSTID structures observed with the imagers were similar to those detected with the GEONET. This fact is expected because 630 nm airglow and TEC are closely related to the *F* region electron density. Such ground-based observations, however, cannot generally provide the altitude profile of electron density fluctuations associated with TIDs, which is essential for the study of physical processes of the interaction between gravity waves and the ionosphere (Hooke, 1968, 1970).

In this paper we analyze the May 22, 1998 MSTID event in detail, focusing on the MSTIDs over Shigaraki (34.85°N, 136.10°E). We first analyze simultaneous data from a 630 nm imager at Shigaraki and GEONET to clarify dynamical features of the MSTIDs and to obtain spatial and temporal relationships between the 630 nm intensity and TEC. Then we use an ionospheric-plasmaspheric electron density model, the Scheffield University Plasmasphere Ionosphere

*Now at Radio Science Center for Space and Atmosphere, Kyoto University, Uji, Kyoto, Japan.
**Now at Interdisciplinary Faculty of Science and Engineering, Shimane University, Matsue, Japan.

Model (SUPIM), to calculate the airglow intensity and TEC variations induced by electron density fluctuations. The model results are compared with the observations.

2. Observations

The 630 nm OI airglow imager at Shigaraki was developed at the Solar-Terrestrial Environment Laboratory, Nagoya University, as part of the Optical Mesosphere Thermosphere Imagers (OMTI) (Shiokawa *et al.*, 1999). This imager, consisting of an all-sky cooled-CCD camera equipped with a 512×512 chip, has a bandwidth of 1.82 nm and a sensitivity of about 0.053 counts Rayleigh^{-1} s^{-1} and automatically provides all-sky images about every 200 s. The imager was calibrated using a 2-m integrating-sphere to know absolute 630 nm intensity in units of Rayleigh (R) (Shiokawa *et al.*, 2000a). The observed emission intensity (I) is contaminated by background sky emission (I_B) that is considered to be independent of wavelength. To get I_B every 30 min, the all-sky imager measures the intensity at 572.5 nm (bandwidth = 1.77 nm) around which no emission bands of molecules and atoms in the atmosphere occur (Shiokawa *et al.*, 1999, 2000a). We hereafter use $I - I_B$ as the intensity of 630 nm airglow.

GPS total electron content data were obtained from GEONET of the Geographical Survey Institute of Japan. The GEONET has about 1000 GPS receivers distributed in Japan (average distance between two receivers $\simeq$25 km) and provides TEC with a time resolution of 30 s. This TEC, however, includes an unknown bias due to satellite and receiver hardware systems. This bias must be removed to get absolute value of TEC (hereafter called GPS-TEC) between the ground and GPS satellite. Otsuka *et al.* (2002) have recently developed a new method to derive approximate GPS-TEC from observed TEC. This method is very useful for the studies of ionospheric and plasmaspheric TEC (Shiokawa *et al.*, 2000b; Balan *et al.*, 2002). The present paper also uses this method to obtain the GPS-TEC.

Geomagnetic activities on May 22, 1998 were a little disturbed because 3-hour Kp indices were 3+, 1, 1, 2−, 2, 3−, 1, 1 ($\Sigma Kp = 14$).

2.1 630 nm airglow

All-sky images obtained at Shigaraki were mapped onto a horizontal plane in a geographic coordinate system by assuming an emission altitude of 250 km around which the volume emission rate of 630 nm airglow has a maximum (see below). Figure 1 displays time variation of the intensity ($I - I_B$) map from 1301 to 1535 UT (from 2201 to 0035 LT) on May 22, 1998. Each map covers 32.50°–37.62°N (570 km) in latitude and 134.00°–139.12°E (470 km) in longitude. In mapping the all-sky images onto geographic coordinates, the images were flat-fielded (Garcia *et al.*, 1997) and not corrected for the Van Rhijn effect that is negligible in Fig. 1 because each map displays the data within a field of view of $\sim$45° around the zenith.

A faint TID, whose phase front extends in the northwest-southeast direction, is discernible in the eastern sky in the 1301 UT map. This TID that propagates at 80 m s^{-1} toward the southwest passes over Shigaraki at about 1323 UT, begins to brighten at about 1331 UT and disappears from the field of view at 1438 UT (see Fig. 2 in more detail). At 1322 UT two TID signatures, one extending from (36.5°N, 137.0°E) to (34.0°N, 139.0°E) and the other around the upper right corner, appear in the northeastern sky: the intensities of these TIDs increase strongly as they propagate toward the southwest at about 80 m s^{-1}. The latter TID passes the zenith of Shigaraki at 1452 UT (160 R; see below) and then becomes faint. At 1408 UT an additional TID appears at around (33.5°N, 139.0°E). As seen in the 1422–1434 UT maps, this TID extends from the northwest to the southeast although its brightness is faint over Shigaraki. A bright TID appears in the upper right corner at 1431 UT. It increases the intensity during the southwestward propagation, but becomes faint before reaching over Shigaraki. Note a very bright spot at around (37.5°N, 135.8°E) in the 1442 UT map that migrates to the southeast along the northern edge of the bright TID and finally merges into the bright TID. This spot is due to cloud. The maps shown in Fig. 1 thus indicate the dynamical growth and decay features of the MSTIDs and suggest that the interaction between gravity waves and ionospheric plasma is not uniform even in a relatively small area (570 km × 470 km) due to the spatial and temporal variabilities of gravity waves and the F region electron density.

The detailed northeast-southwest propagation characteristics of TIDs are discernible in Fig. 2 which gives time variation of the emission intensity from 1300 to 1600 UT along the NE (36.5°N, 138.0°E)–SW (32.5°N, 134.0°E) direction ($\sim$600 km) shown in Fig. 1. Shigaraki is located close to the 300 km point. A series of MSTIDs propagating from the northeast to the southwest are clearly seen until 1530 UT although the intensity varies in time and space. The strongest intensity with 200 R or more appears at around 1420 UT in the southwestern sky. It is interesting to note that (1) all the airglow bands are enhanced during 1400–1500 UT, and (2) the faint TIDs that have propagated from the north intensify in the south of Shigaraki after 1400 UT while the bright TIDs that have also propagated from the north become faint near Shigaraki after 1500 UT. On this night, the middle and upper atmosphere (MU) radar observed electron density over Shigaraki (see figure 7 of Saito *et al.*, 2002). The F layer peak altitude descended from 380 km at 1300 UT to 360 km at 1345 UT after which, unfortunately, strong sporadic E layer prevented the F region observations below 400 km. The sporadic E layer disappeared at about 1545 UT at which time the F layer peak altitude was 410 km. Then the peak altitude descended gradually to attain to 330 km at 1700 UT. It is thus inferred that (1) the airglow enhancements during 1400–1500 UT were caused by the downward movement of the F region and (2) its decay after 1500 UT was due to the F region uplift.

The physical parameters of the MSTIDs estimated from Fig. 2 are: horizontal wavelength = 200–300 km, period = 30–50 min, and phase velocity = 80–100 m s^{-1}. The simple dispersion relation of internal gravity waves given by Hines (1960) is $(L_x/L_z)^2 = (T/T_b)^2 - 1$ where L_x and L_z are the horizontal and vertical wavelengths, respectively, T is the wave period, and T_b is the Brunt-Väisälä period ($\simeq$15 min in the F region). This relation yields the vertical wavelength of the order of 100 km.

Time variation of I_B (background 572.5 nm intensity) at the zenith of Shigaraki is shown in the upper panel in

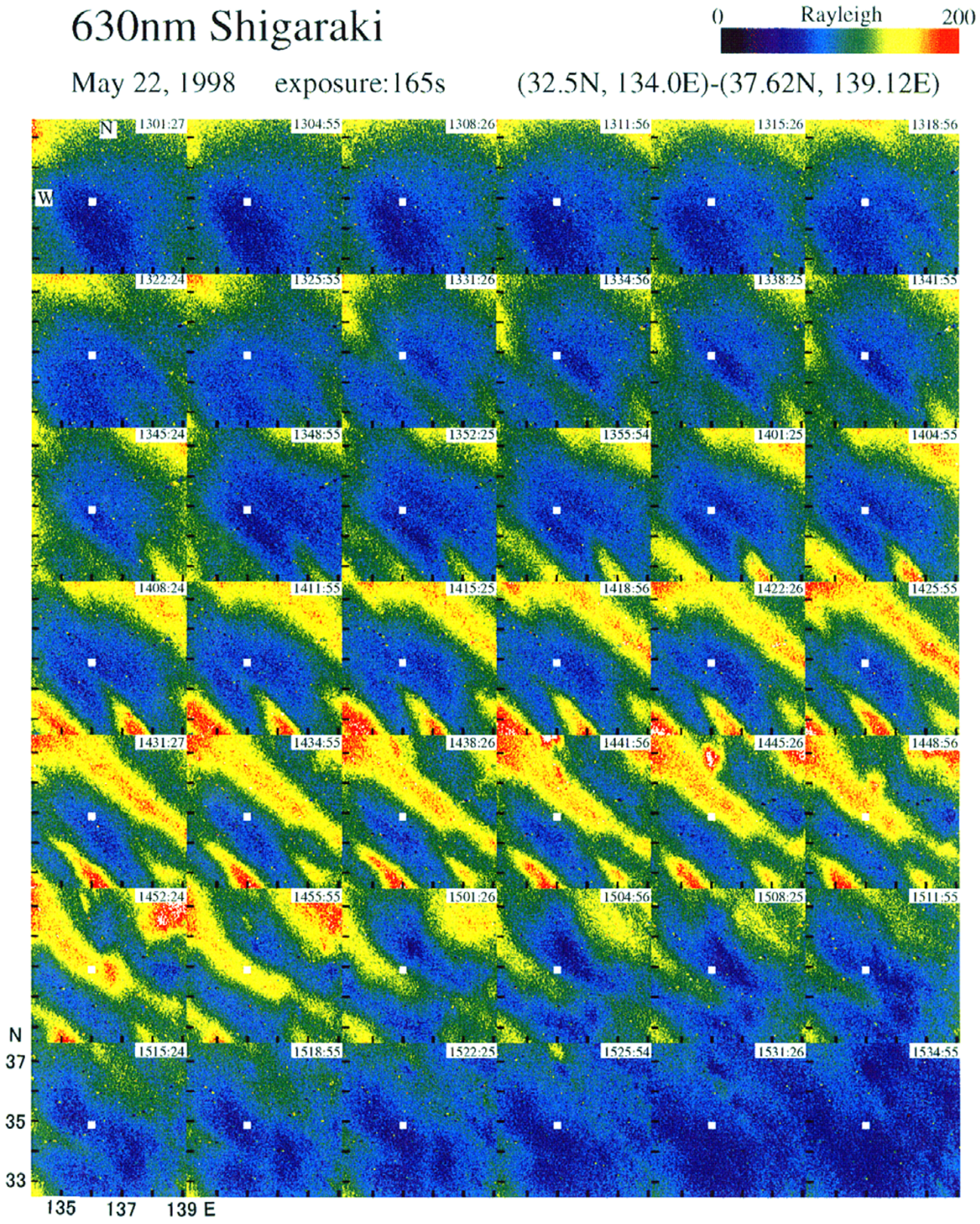

Fig. 1. Time variation of 630 nm intensity map in geographic coordinates (32.50°–37.62°N, 134.00°–139.12°E) from 1301 to 1535 UT (from 2201 to 0035 LT) on May 22, 1998. An emission altitude of 250 km is assumed to map the all-sky images into geographic coordinates. The position of Shigaraki is marked by the white square.

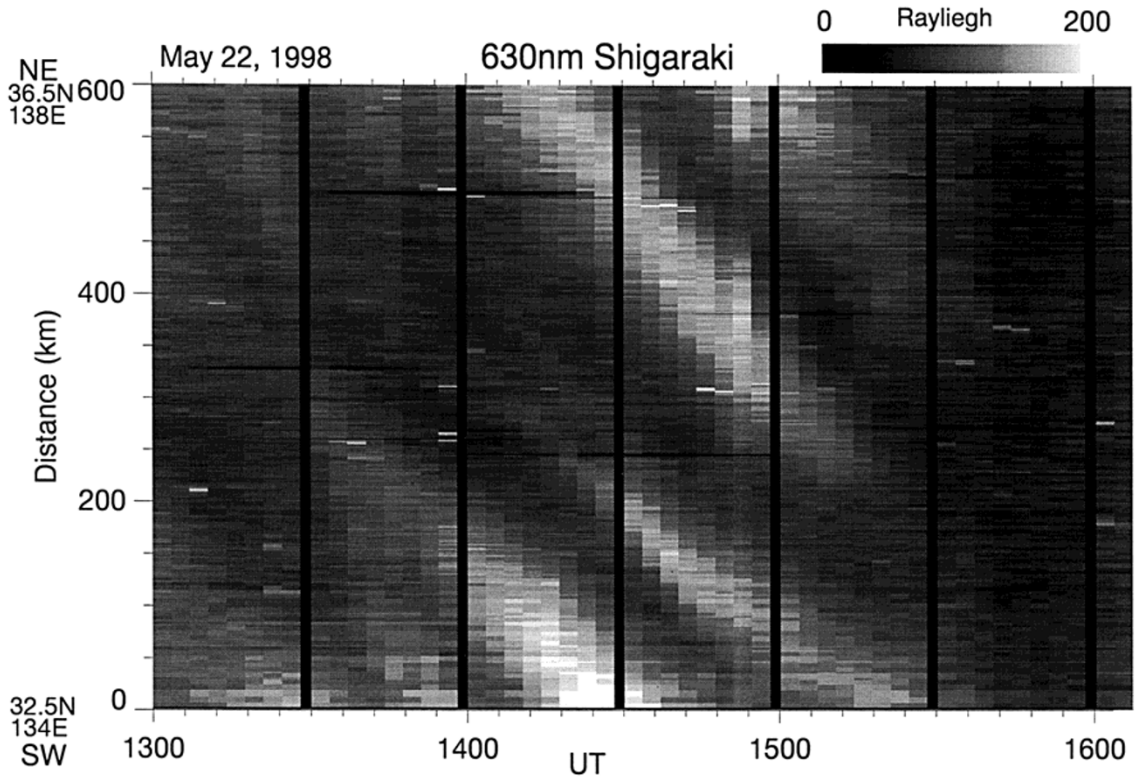

Fig. 2. Time variation of 630 nm intensity along the NE (36.50°N, 138.0°E)–SW (32.50°N, 134.0°E) direction (∼600 km) shown in Fig. 1. The thick vertical bars denote the times when the background 572.5 nm intensity was measured. Shigaraki is located close to the 300 km point.

Fig. 3. The lower panel shows time variation of $I - I_B$ (630 nm emission intensity from the ionosphere). This intensity varies between 60 and 80 R with fluctuation amplitudes of a few-6 R (i.e., relative amplitudes of a few-8%) during 1300–1620 UT except for the period between 1430 and 1500 UT when the intensity is largely enhanced up to 160 R (almost twice the quiet value of 80 R). This enhancement is obviously related to the passage of the brightest 630 nm region over Shigaraki (Figs. 1 and 2). The rapid intensity increase after 1630 UT is due to cloudy sky.

2.2 GPS-TEC

Simultaneous observations of GPS-TEC were made at a receiving station in Nagoya (35.17°N, 136.97°E), 85 km east of Shigaraki. Figure 4(a) shows the 630 nm intensity maps (every 15 min) picked up from Fig. 1. Also marked are 300-km subionospheric points of the ray paths from two GPS satellites (PRN#08 and 09) to the Nagoya receiver. The subionospheric points move gradually toward ENE while the TIDs propagate toward SW.

Time variation of vertical GPS-TEC at the subionospheric point for each GPS ray path is shown in Fig. 5(a). Vertical GPS-TEC is derived by applying the Otsuka *et al.* (2002) method and is defined as (slant TEC) × S. Here, S is the slant factor that is determined as a ratio of the assumed ionospheric thickness (250 km) to the ray path length between the 300 and 550 km altitudes. The vertical TECs in Fig. 5(a) are highly variable in space and time, reflecting the fact that the ray paths cross the highly structured ionosphere. Comparison of Figs. 5(a) and 4(a) indicates the following facts: (1) when the GPS ray paths lie within the bright (dark) air-

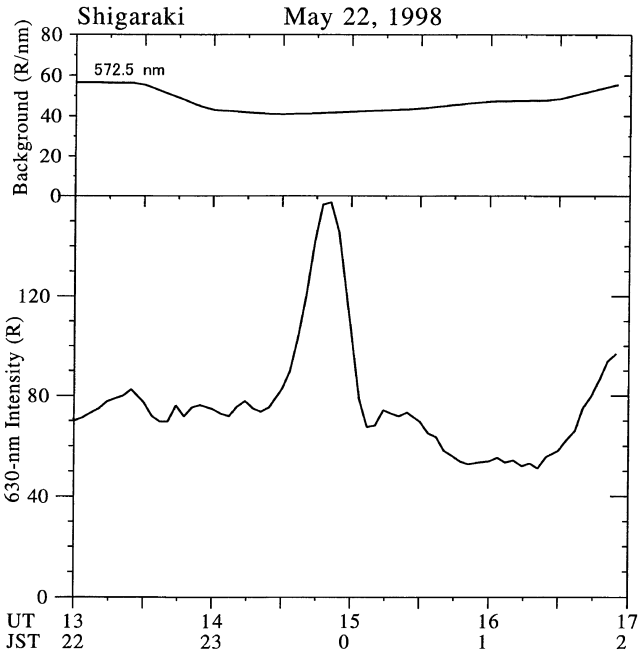

Fig. 3. Time variations of (upper) background 572.5 nm intensity (every 30 min) and (lower) 630 nm intensity at the zenith of Shigaraki from 1300 to 1700 UT (from 2200 to 0200 LT). The 630 nm intensity enhancement after 1620 UT is due to cloudy sky.

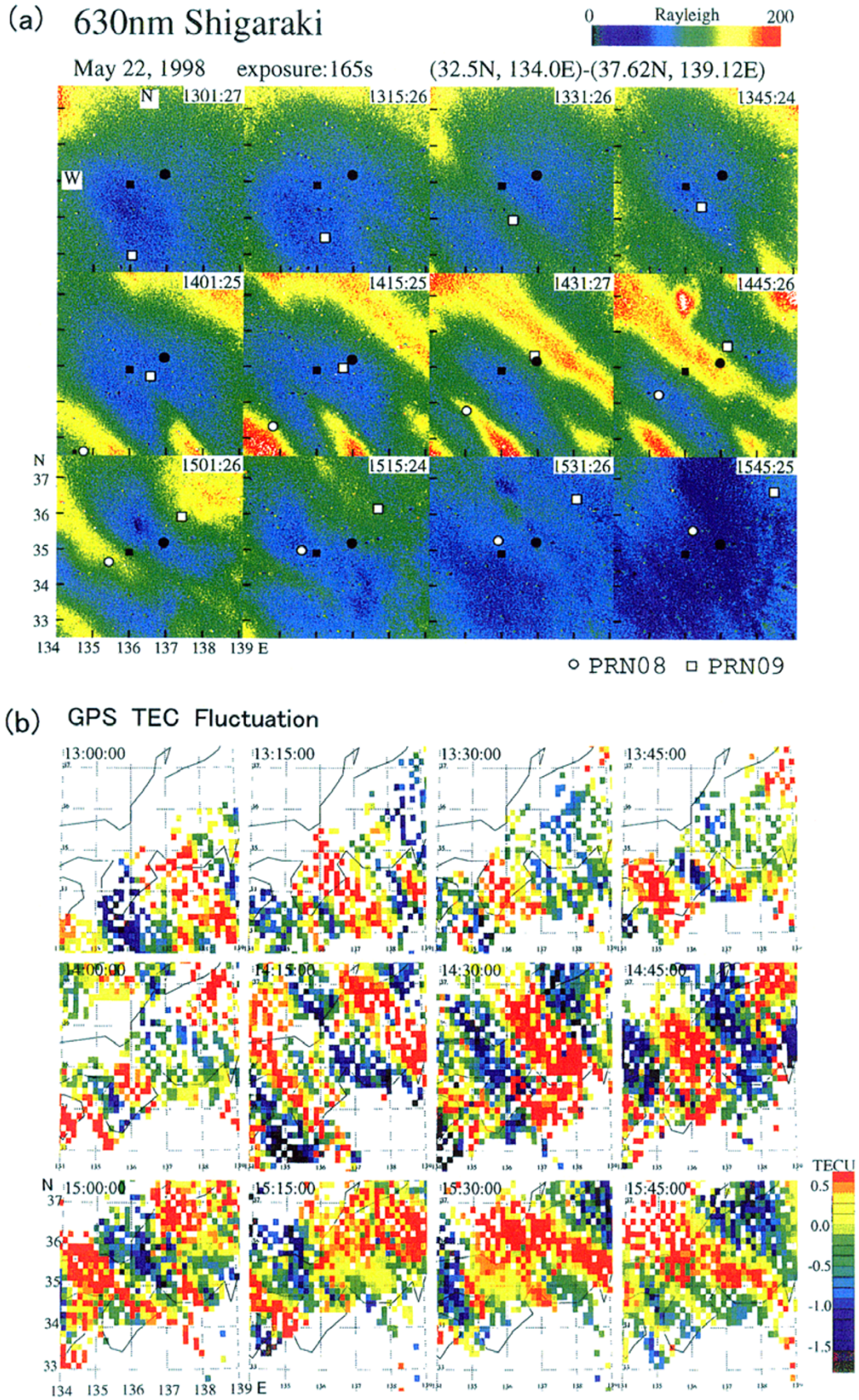

Fig. 4. (a) Time variation of 630 nm intensity maps in geographic coordinates. Also shown are the 300-km subionospheric points of ray paths from two GPS satellites to a receiver in Nagoya. The bright spot at around (37.0°N, 136.0°E) at 1445 UT is due to cloud. The positions of Shigaraki and Nagoya are marked by the black square and circle, respectively. (b) GPS-TEC fluctuation maps at the same times as Fig. 4(a).

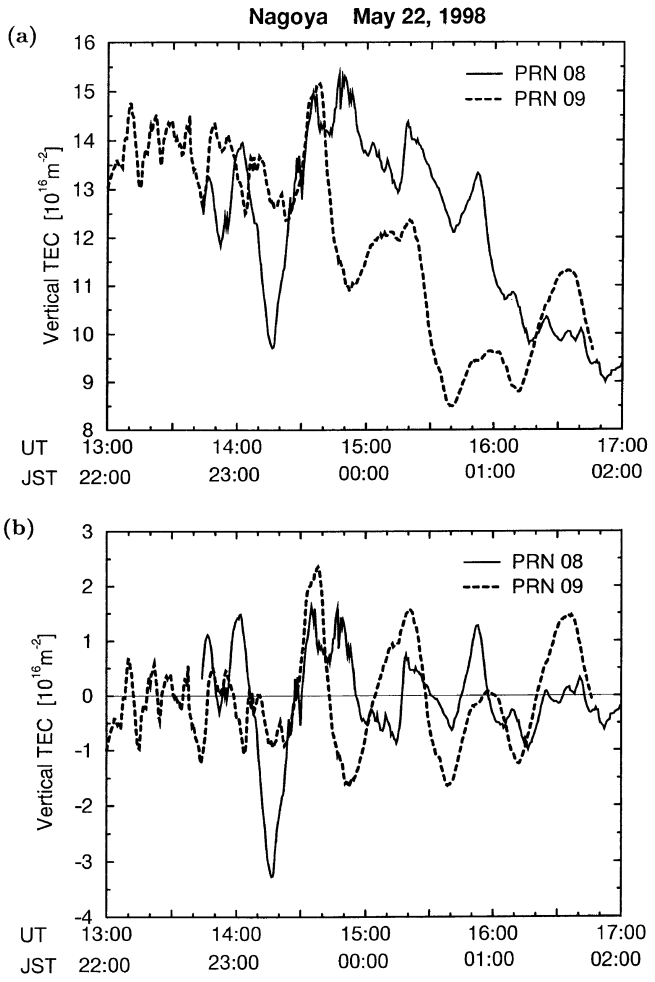

Fig. 5. (a) Time variations of vertical GPS-TEC observed in Nagoya using two GPS satellites. (b) Deviation of the vertical GPS-TEC from two-hour running mean for each GPS.

glow regions, the vertical TECs are enhanced (decreased), suggesting one-to-one correspondence between the airglow intensity and TEC variations (that is, the airglow intensity is strongly dependent on the F region electron density); (2) between 1330 and 1530 UT when the TIDs are active (Fig. 2), the average vertical GPS-TECs are roughly 14–15 TEC units (TECU; 1 TECU $= 10^{16}$ electrons m^{-2}) within and around the enhanced airglow regions and are roughly 11–13 TECU around the suppressed airglow regions. Figure 5(b) shows deviation of GPS-TEC from two-hour running mean for each GPS satellite. Wavy structures with periods of 10–40 min can be seen. Fluctuation amplitudes are about 0.5 TECU (a few % of the background) in and around the weak airglow regions and are about 2.5 TECU (20%) in the brightest regions. Note that our TEC fluctuation amplitudes are larger than those of MSTIDs studied by Saito *et al.* (1998).

2.3 Comparison of 630 nm intensity and GPS-TEC

We constructed a spatial distribution of GPS-TEC fluctuations (deviations from two-hour running mean) by applying the Saito *et al.* (1998) method to GPS-TEC data available from the GPS receivers located in the central part of Japan. The GPS-TEC fluctuation maps at the same times as Fig. 4(a) are displayed in Fig. 4(b) where the data with satellite elevation angles larger than 45° are used. Comparison of Figs. 4(a) and 4(b) indicates that the following features: (1) before 1500 UT there is clear spatial coincidence between the bright (dark) airglow regions and the positive (negative) TEC fluctuation regions; (2) after 1500 UT the airglow intensities are generally faint whereas the TEC fluctuation amplitudes keep high values. The latter fact suggests that the high-amplitude electron density fluctuation regions ascend to the higher altitudes after 1500 UT where the 630 nm emission rate is low. This ascent can be related to the upward motion of the F region peak as inferred from the MU radar observations (Subsection 2.1).

Figure 6 shows the TEC and 630 nm fluctuation distributions at 1430 UT along the NE (36.5°N, 138.0°E)–SW (32.5°N, 134.0°E) direction (∼600 km) shown in Fig. 4. It is clear that the enhanced (depleted) TEC fluctuation regions coexist well with the enhanced (depleted) airglow regions; that is, a 70 R variation (from 150 to 80 R) at distances between 200 and 300 corresponds to 1 TECU and a 90 R variation (from 80 to 170 R) between 300 and 500 km does to 1.5 TECU. Such correlation is expected from the possible relationship between enhancements in the F region electron density and 630 nm intensity. In Subsection 2.1 we have estimated the TID vertical wavelength of about 100 km. If this were the case, there should appear a significant phase difference in time and space between the airglow intensity and TEC. Our observations indicate that the apparent vertical wavelength was far longer than 100 km.

GEONET measures TEC from one GPS satellite simultaneously at many receiving stations. This capability enables us to construct a time history of GPS-TEC at a fixed location. Figure 7(a) displays time variation of GPS-TEC at the zenith of Shigaraki observed with PRN#09 whose 400-km subionospheric points were close to Shigaraki between 1310 and 1510 UT. Comparison between Figs. 2 and 7(a) indicates that (1) the small GPS-TEC maxima at around 1330 and 1410 UT correspond well to the weak airglow regions, and (2) GPS-TEC reaches a maximum of 13 TECU at around 1450 UT when the brightest airglow band passes over Shigaraki. Figure 7(b) shows GPS-TEC deviation from two-hour running mean together with the 630 nm intensity (lower panel in Fig. 3). A 80 R enhancement centered at around 1452 UT corresponds well to the enhancement of 3 TECU (that is, no phase shift between the airglow intensity and TEC), and the small-amplitude fluctuations in the 630 nm intensity (≤5 R) before 1430 UT are correlated with those in GPS-TEC (≤1 TECU).

2.4 Summary of observations

The observations at Shigaraki are summarized as follows:

1. A series of MSTIDs propagating from NE to SW were detected in the 630 nm airglow maps. TID parameters are: horizontal wavelength = 200–300 km, period = 30–50 min, and phase velocity = 80–100 m s^{-1}.

2. The MSTIDs grew and decayed even in a small area of 570 km (latitude) × 470 km (longitude) due to spatial and temporal variabilities of gravity waves and/or electron density. There was one-to-one correspondence between the airglow intensity and GPS-TEC before 1500 UT, but after 1500 UT this correspondence was a little unclear, perhaps

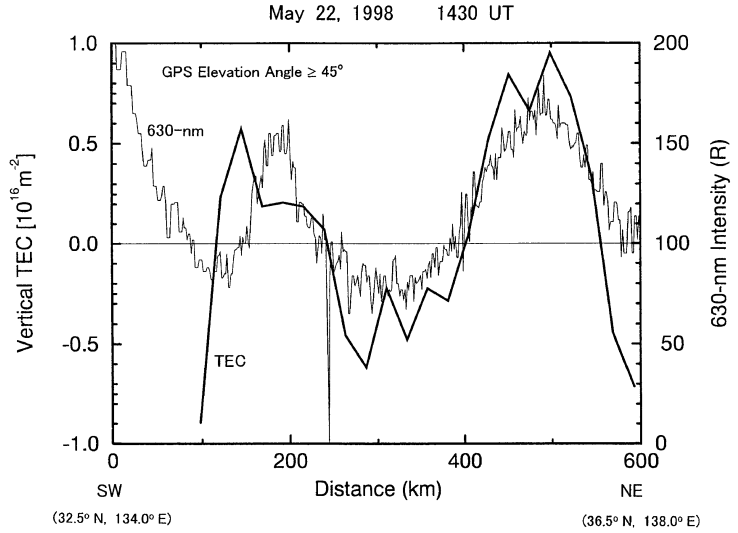

Fig. 6. Spatial profiles of 630 nm intensity and vertical GPS-TEC deviation from two-hour running mean along the NE (36.5°N, 138.0°E)–SW (32.5°N, 134.0°E) direction (∼600 km) shown in Fig. 4.

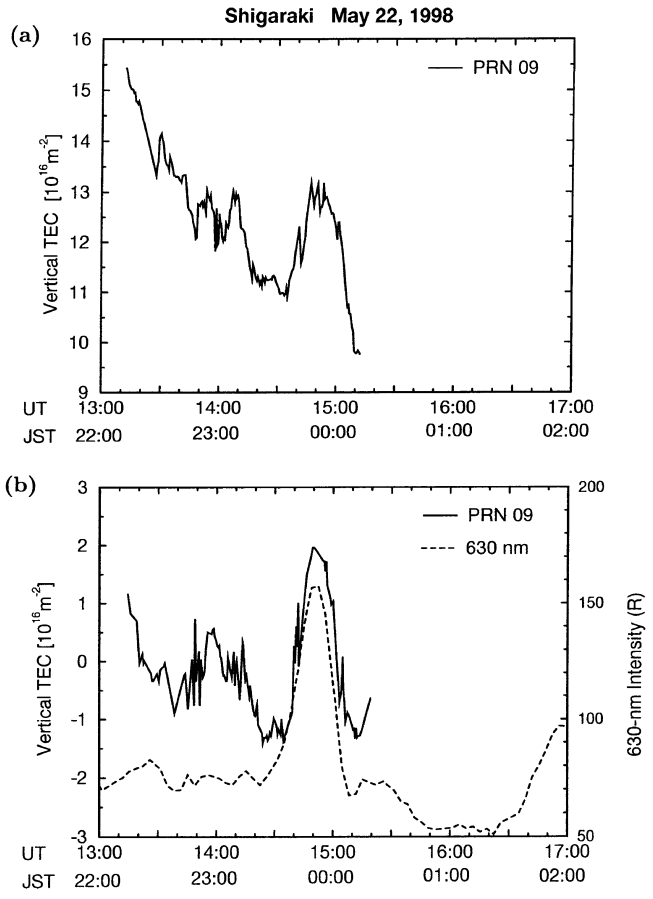

Fig. 7. (a) Time variation of vertical GPS-TEC at the zenith of Shigaraki derived from GPS PRN#09 measurements. (b) Deviation of the vertical GPS-TEC from two-hour running mean and the 630 nm intensity shown in Fig. 3.

because of upward motion of the F layer.

3. Absolute airglow intensity between 1300 and 1620 UT was 60–80 R with fluctuation amplitudes of a few-6 R (relative amplitudes of a few-8%). The airglow bands in the Shigaraki field of view were simultaneously enhanced between 1400 and 1500 UT, perhaps due to downward movement of the F layer. This movement is expected from the simultaneous MU radar observations.

4. Average vertical GPS-TECs were 14–15 TECU within and around enhanced airglow regions and about 11–13 TECU around suppressed airglow regions. GPS-TEC showed clear wavy structures with periods of 10–40 min and fluctuation amplitudes of 0.5–2.5 TECU (relative amplitudes of a few-20%). The amplitude became higher with increasing period.

5. In particular, when the brightest airglow band passed over Shigaraki, the airglow intensity and vertical GPS-TEC increased by 80 R and 3 TECU, respectively.

3. Modeling of Airglow and GPS-TEC

Our ground-based observations give no information on the altitude profiles of the 630 nm emission rate $V_{630}(z)$ and electron density $N_e(z)$. Modeling work is necessary to understand the relationships between these quantities and also between V_T ($= \int V_{630}\, dz$) and TEC ($= \int N_e\, dz$) that are measured on the ground. In this paper we use the SUPIM to model the background $N_{e0}(z)$ (Balan and Bailey, 1995). Then, we add an altitude-dependent electron density perturbation to N_{e0} to calculate 630 nm intensity and GPS-TEC variations and compare the results with the observations.

3.1 The SUPIM model

Using SUPIM we model $N_{e0}(z)$ in the background ionosphere and plasmasphere at altitudes between 150 and 20,200 km (GPS altitude) at 1400 UT (2300 LT) on May 22, 1998 at the zenith of Shigaraki. Some parameters input into SUPIM are: geomagnetic latitude = 26°N, geographic longitude = 135°E, 10.7-cm solar flux (F10.7) = 101, and

10.7-cm solar flux averaged over three solar rotations (81 days) = 85. Neutral densities and temperatures are obtained from MSIS86 (Hedin, 1987). North-south neutral winds in SUPIM are taken from the HWM90 model (Hedin *et al.*, 1991). Using these parameters we calculated the 630 nm intensity and GPS-TEC over Shigaraki and found that these are 43.5 R and 18.8 TECU, respectively, which are different from the observed values of about 80 R and 11–15 TECU. Then we reduced the HWM90 N–S wind during 1100–2000 UT to 25% to obtain the results rather consistent with the observations.

Figure 8 plots altitude profile of the SUPIM electron density at 1400 UT. This profile gives a GPS-TEC of 16.0 TECU that is a little larger than the value of 11–15 TECU observed over Shigaraki at 1300–1500 UT (Fig. 7(a)). The profile below 500 km is enlarged in Fig. 9 where the O^+ profile is also shown. The electron density has a maximum of 2.8×10^5 cm^{-3} at 300 km. The MU radar observations on this night showed that the F layer peak altitude descended from 380 km at 1300 UT to 360 km at 1345 UT (see Subsection 2.1).

3.2 630 nm emission rate

To calculate the 630 nm OI emission rate V_{630} (photons cm^{-3} s^{-1}) using SUPIM, we adopt the following equation given by Sobral *et al.* (1993).

$$V_{630} = \frac{0.756 f(^1\mathrm{D}) k_3 [\mathrm{O_2}] N_e}{(N_e/[\mathrm{O^+}])\,[1 + (\mathrm{k_2[N_2]} + \mathrm{k_5[O_2]} + \mathrm{k_6 N_e} + \mathrm{k_7[O]})/\mathrm{A_{1D}}]}, \quad (1)$$

where $f(^1\mathrm{D}) = 1.1$ is the O(^{1}D) quantum yield in O_2^+ dissociative recombination and $\mathrm{A_{1D}} = 7.45 \times 10^{-3}$ s^{-1} is the Einstein transition coefficient for O(^{1}D) state. The k_i values are the reaction coefficients of the following reactions:

$$\mathrm{O_2 + O^+ \rightarrow O_2^+ + O} \quad (k_3 = 1.06 \times 10^{-11}\ \mathrm{cm^3 s^{-1}}), \quad (2)$$

$$\mathrm{O(^1D) + N_2 \rightarrow O(^3P) + N_2} \quad (k_2 = 2.30 \times 10^{-11}\ \mathrm{cm^3 s^{-1}}), \quad (3)$$

$$\mathrm{O(^1D) + O_2 \rightarrow O(^3P) + O_2} \quad (k_5 = 3.20 \times 10^{-11}\ \mathrm{cm^3 s^{-1}}), \quad (4)$$

$$\mathrm{O(^1D) + e \rightarrow O(^3P) + e} \quad (k_6 = 6.60 \times 10^{-10}\ \mathrm{cm^3 s^{-1}}), \quad (5)$$

$$\mathrm{O(^1D) + O \rightarrow O(^3P) + O} \quad (k_7 = 9.2 \times 10^{-13}\ \mathrm{cm^3 s^{-1}}). \quad (6)$$

Figure 10 plots altitude profiles of the deactivation rates of O(^{1}D) appearing in Eq. (1) together with the $k_3[\mathrm{O_2}]$ profile. The estimated altitude profile of V_{630} is plotted in Fig. 9. The emission layer exists at altitudes between 150 and 400 km where the $k_2[\mathrm{N_2}]$ term in the denominator in Eq. (1) is predominant, and V_{630} reaches 8 photons cm^{-3} s^{-1} at 250 km, being 50 km (about one scale-height) below the F layer peak (300 km). Using a two-station triangulation method, Kubota *et al.* (2000) derived the 630 nm emission altitude of 260 ± 10 km at 1420 UT on May 22. This altitude is very consistent with our result (250 km).

The total emission intensity observed on the ground is given by

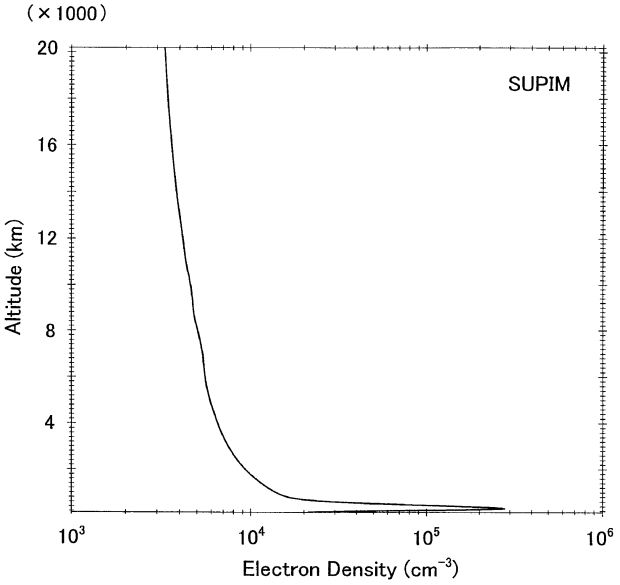

Fig. 8. Electron density profile at altitudes between 150 and 20,200 km over Shigaraki at 1400 UT on May 22, 1998 derived from SUPIM.

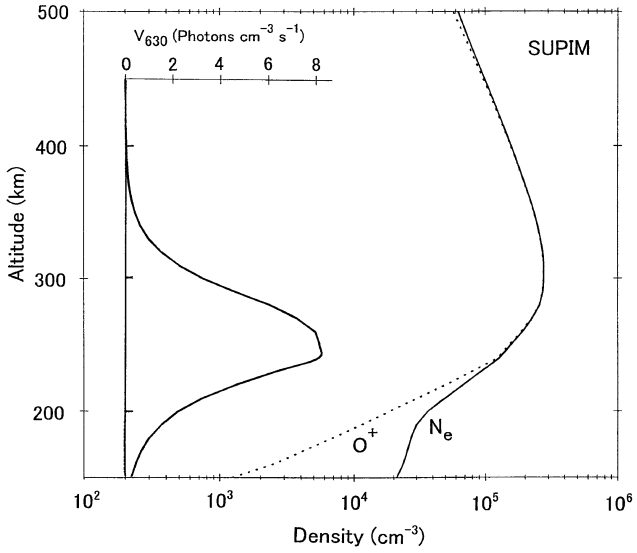

Fig. 9. Electron and O^+ density profiles at altitudes between 150 and 500 km over Shigaraki at 1400 UT on May 22, 1998 derived from SUPIM. Profile of 630 nm volume emission rate is also plotted.

$$V_T = \int V_{630}\, dz \ (\mathrm{photons\ cm^{-2}\ s^{-1}}) = 10^{-6} \int V_{630}\, dz \ (\mathrm{Rayleigh}). \quad (7)$$

Substituting the V_{630} profile in Eq. (7) gives $V_T = V_{T0} =$ 71.4 R that is comparable to 75 R observed at 1400 UT.

3.3 TID-induced airglow and GPS-TEC variations

A TID accompanies spatial and temporal changes of electron density (Hooke, 1968). Porter and Tuan (1974) gave a complicated functional form of the density change. However, we estimate the airglow and GPS-TEC values when a half-wavelength sinusoidal fluctuation along the altitude (z)

Table 1. Absolute fluctuation amplitudes of 630 nm total emission intensity ($|\Delta V_T|$) and GPS-TEC ($|\Delta GTEC|$) as a function of A (± 0.2, ± 0.5, $+1.0$, and $+2.0$), h (150 and 250 km), and z ($z_0 \leq z \leq z_0 + h$; $z_0 = 150$, 200, and 250 km).

	$h = 150$ km			$h = 250$ km		
$\|A\|$	z (km)	$\|\Delta V_T\|$ (R)	$\|\Delta GTEC\|$ (TECU)	z (km)	$\|\Delta V_T\|$ (R)	$\|\Delta GTEC\|$ (TECU)
0.20	150–300	9.2	0.2	150–400	12.3	0.6
0.20	200–350	9.9	0.4	200–450	8.3	0.7
0.20	250–400	4.0	0.5	250–500	2.8	0.6
0.50	150–300	22.8	0.5	150–400	30.7	1.5
0.50	200–350	24.8	1.0	200–450	20.7	1.7
0.50	250–400	9.9	1.2	250–500	6.9	1.5
1.00	150–300	45.8	1.0	150–400	61.5	2.9
1.00	200–350	49.6	2.0	200–450	41.4	3.4
1.00	250–400	19.8	2.5	250–500	13.9	3.0
2.00	150–300	90.1	2.0	150–400	120.1	5.9
2.00	200–350	97.5	4.0	200–450	81.1	6.8
2.00	250–400	38.5	4.7	250–500	27.2	6.1

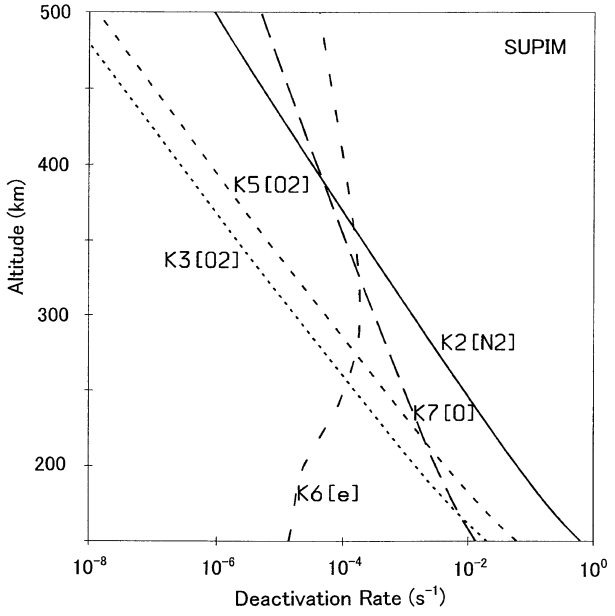

Fig. 10. Altitude profiles of deactivation rates of $O(^1D)$ in Eq. (1). $k_3[O_2]$ is also plotted.

is added to the background electron density (Thome, 1964; Evans *et al.*, 1983). Although such a simple fluctuation may oversimplify the realistic one that was introduced by Porter and Tuan (1974) and Porter *et al.* (1974), it gives us an important clue to the relationship among the electron density, airglow, and TEC variations.

The electron density profile in our model is given by

$$N_e(z) = N_{e0}(z)\{1 + A \sin[(z - z_0)\pi/h]\} : \quad z_0 \leq z \leq z_0 + h, \tag{8}$$

$$N_e(z) = N_{e0}(z) : \text{ otherwise}, \tag{9}$$

where A is the maximum fluctuation amplitude, h is the half of the fluctuation wavelength, and z_0 is the lowest altitude of the fluctuation region. Substituting Eqs. (8) and (9) into Eq. (1) gives the altitude profile of V_{630} including the fluctuation. In the calculations we neglect the TID (gravity wave)-induced variations of the neutral gas densities in Eq. (1). This because, as calculated in Appendix A, the variations of these densities are less than the variation in the electron density except for TIDs propagating nearly perpendicular to the geomagnetic field: in this case the electron density variation is largely suppressed. See, for example, a paper by Hooke (1968) for the neutral density perturbations due to gravity waves. Also, for simplicity we use the background values for the $N_e/[O^+]$ term in Eq. (1).

We calculated V_T and GPS-TEC for various combinations of A, h, and z_0; that is, $A = \pm 0.2$, ± 0.5, $+1.0$, and $+2.0$; $h = 150$ and 250 km; $z_0 = 150$, 200, and 250 km. The h values adopted here are larger than 50 km corresponding to a vertical wavelength of 100 km (Subsection 2.1). As noted above, we need h far larger than 50 km to explain no appreciable phase shift between the ariglow and GPS-TEC (Figs. 6 and 7(b)). We denote V_T as V_{T0} (background; 71.4 R) + ΔV_T (fluctuation) and *GTEC* (GPS-TEC) as $GTEC_0$ (background; 16.0 TECU) + $\Delta GTEC$. The results of ΔV_T and $\Delta GTEC$ are summarized in Table 1. The calculations indicate that for positive (negative) A less than 1.0, ΔV_T and $\Delta GTEC$ have positive (negative) values, and moreover that their absolute values are almost equal for the same positive and negative A. So only the absolute values

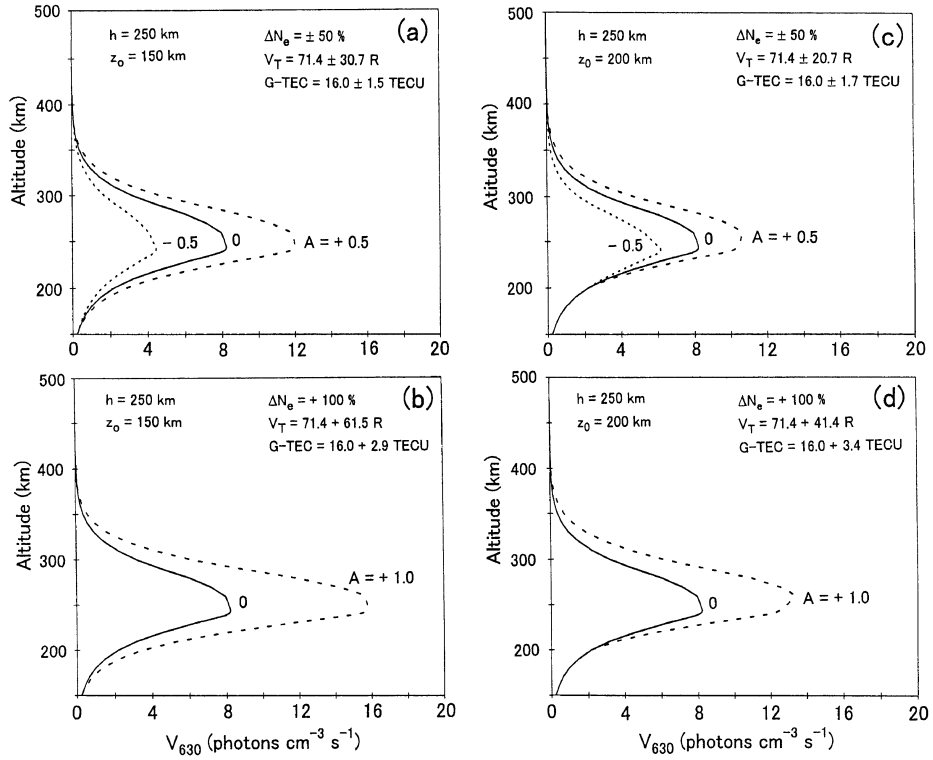

Fig. 11. Altitude profiles of V_{630} perturbed by electron density fluctuations with (a) $h = 250$ km, $z_0 = 150$ km, and $A = \pm 0.5$ ($\Delta N_e = \pm 50\%$), (b) $h = 250$ km, $z_0 = 150$ km, and $A = +1.0$ ($\Delta N_e = +100\%$), (c) $h = 250$ km, $z_0 = 200$ km, and $A = \pm 0.5$, and (d) $h = 250$ km, $z_0 = 200$ km, and $A = +1.0$. Profile of V_{630} for $A = 0$ is also shown in each panel. Numerical values of $V_T = V_{T0} + \Delta V_T$ and $GTEC = GTEC_0 + \Delta GTEC$ are listed.

of A, ΔV_T, and $\Delta GTEC$ are listed in Table 1. The general tendencies recognized from Table 1 are: (1) V_T is most enhanced when the electron density fluctuations with larger amplitude and wider altitude-extent appear at altitudes covering the peak altitude (250 km) of the 630 nm emission layer, (2) GPS-TEC is most enhanced when the electron density fluctuations exist around the F region peak altitude (300 km). Of course, these characteristics depend on the assumed sinusoidal electron density variation along z.

As examples, Figs. 11(a) and 11(b) show altitude profiles of V_{630} for $h = 250$ km, $z_0 = 150$ km, and $A = \pm 0.5$ (Fig. 11(a)) and $+1.0$ (Fig. 11(b)). In Fig. 11(a), V_T is 71.4 ± 30.7 R and GPS-TEC is 16.0 ± 1.5 TECU, while in Fig. 11(b), V_T is $71.4 + 61.5$ R and GPS-TEC is $16.0 + 2.9$ TECU. In these figures, V_T is maximized at 250 km. This altitude is almost steady for other h, z_0, and A combinations. Figures 11(c) and 11(d) display V_{630} altitude profiles for $z_0 = 200$ km (that is, the fluctuation region ascends by 50 km compared wtih Figs. 11(a) and 11(b)) while the other parameters are the same as those in Figs. 11(a) and 11(b). V_T is still maximized at about 250 km while ΔV_T decreases and $\Delta GTEC$ increases.

3.4 Comparison between observations and modeling

Small-amplitude airglow region: The airglow intensities over Shigaraki were 60–80 R with fluctuation amplitudes of a few-6 R. Our calculations show a background intensity of 71.4 R that is comparable to the observed value. The observed fluctuation amplitudes are also comparable to the values calculated for the electron density fluctuations with $|A| = 0.2$ and $150 \leq z \leq 300$ km (see Table 1). The observed GPS-TEC of 11–15 TECU is less than the model value of 16.0 TECU. The observed TEC fluctuation amplitudes are about 0.5 TECU, again consistent with the electron density fluctuations with $|A| = 0.2$.

Large-amplitude airglow region: The observed airglow intensity and GPS-TEC were enhanced by 80 R and 3 TECU, respectively, above the background when the brightest airglow region passed over Shigaraki. Table 1 suggests that such high values are possible when A is about 1.5 and also the maximum electron density fluctuation appears below the 300 km altitude.

As noted in Subsection 2.3, after 1500 UT the airglow intensities are low whereas the TEC fluctuation amplitudes are still high. Table 1 tells that such situation is possible when the main electron density fluctuation regions exist above, say, 250 km.

4. Discussion and Conclusions

We observed a series of southward-propagating MSTIDs over Shigaraki on the night of May 22, 1998. Background airglow intensity and GPS-TEC were 60–80 R and 11–15 TECU, respectively, and amplitudes of TID-associated airglow and GPS-TEC fluctuations were a few-6 R and 0.5–2.5 TECU, respectively. These amplitudes reached 80 R and 3 TECU when a bright airglow band passed over Shigaraki. This bright region came from the north of the Japanese island as observed by Kubota *et al.* (2000) and decayed in the south of Shigaraki. Saito *et al.* (2001) observed GPS-TEC

fluctuations with amplitudes less than 2 TECU on this night over Japan. Our results over Shigaraki are rather consistent with these observations.

Decay and enhancement of MSTIDs were clearly detected within the Shigaraki field of view (470 km × 570 km), suggesting that amplitudes of atmospheric gravity waves and interaction process between gravity waves and F region plasma were highly variable in space and time.

Enhanced (depleted) airglow regions are well coincident with enhanced (depleted) GPS-TEC regions, which means that 630 nm intensity is strongly dependent on the F region electron density distribution. Brown and Steiger (1972) observed phase differences in time between fluctuations of 630 nm intensity and ionospheric TEC associated with large-scale TIDs. Porter *et al.* (1974) predicted such phase differences for large-scale TIDs. Our observations of MSTIDs, however, do not indicate such behavior. We have estimated a vertical wavelength of about 100 km from a simple dispersion relation of gravity waves. This means that the gravity wave has a phase shift of 180° over 50 km in altitude to produce an appreciable phase difference between the 630 nm intensity and GPS-GTEC, which is inconsistent with our result that indicates the apparent vertical wavelength far longer than 100 km. One possibility to explain this inconsistency is that under highly variable ionospheric conditions we cannot use the simple dispersion relation to derive the vertical wavelength. To resolve the problem simultaneous observations of F region plasma density distribution, airglow intensity, and TEC are needed.

We have used SUPIM to calculate theoretical relationship between 630 nm intensity and GPS-TEC. The results are reasonably consistent with the observations. The fluctuation amplitudes of airglow and GPS-TEC in small-amplitude airglow regions are explained by an electron density fluctuation of about 20% occurring around an altitude of 250 km where the 630 nm emission is maximized. Highly enhanced airglow intensity (80 R) and GPS-TEC (3 TECU) within large-amplitude airglow region seems to be caused by an electron density fluctuation of about 150% appearing below the 300 km altitude. The 80 R enhancement is also possible when the F layer simply descends down to lower altitudes to increase the electron density at around 250 km; in this case, however, no GPS-TEC enhancement is expected. Our suggestion that the altitude range of the electron density fluctuations is mainly below the F region peak is consistent with the result of Saito *et al.* (2002). They have found from incoherent scatter observations of the MU radar that electron density variations associated with MSTIDs occurred mainly at and below the F region peak.

It is expected from the current modeling works that when electron density fluctuations exist at altitudes higher than 250 km, airglow intensity is low but TEC fluctuation is high. Our observations indicate that such situation is possible.

Acknowledgments. We are grateful to the staff of Radio Science Center for Space and Atmosphere of Kyoto University for their kind support to routine OMTI observations at Shigaraki. GPS data were supplied from the Geographical Survey Institute of Japan. This work was supported by Grant-in-Aid for Scientific Research of the Ministry of Education, Culture, Sports, Science and Technology of Japan (11440145).

Appendix A. Electron and Neutral Density Perturbations

For internal gravity waves, the first-order perturbation (ΔN_e) of the electron density from its unperturbed value (N_{e0}) caused by the neutral atmospheric motion (**U**) is given by (Hooke, 1970)

$$\Delta N_e = \frac{N_{e0}(\mathbf{U}\cdot\mathbf{I}_b)(\mathbf{k}\cdot\mathbf{I}_b)}{\omega}, \tag{A.1}$$

where **k** is the wave vector, $\mathbf{I}_b$ is a unit vector along the geomagnetic field, and ω is the wave frequency. Eq. (A.1) is valid under the condition $4k_z^2 \gg 1/H^2$ where k_z is the vertical component of **k** and H is the neutral atmospheric scale height (∼50 km in the F region). This condition is fulfilled for the vertical wavelengths less than 630 km. In a coordinate system with x axis directed southward and z axis directed upward in the northern hemisphere, Eq. (A.1) is rewritten as

$$\frac{\Delta N_e}{N_{e0}} = \frac{U\cos(\theta+I)\cos(\phi+I)}{V_{ph}}, \tag{A.2}$$

where $V_{ph}(=\omega/k)$ is the phase velocity, I is the magnetic dip angle (downward positive), θ is the angle between x axis and **k**, and ϕ is the angle between x axis and **U**. For a southward-propagating gravity wave, both **k** and **U** are in the $x-z$ plane and **k** is directed southward and downward. The asymptotic dispersion relation $U_z/U_x \simeq -k_x/k_z$ (Hines, 1960), where $U_x = U\cos\phi$, $U_z = -U\sin\phi$, $k_x = k\cos\theta$, and $k_z = -k\sin\theta$, yields $\theta-\phi = \pm 90°$. Hence, Eq. (A.2) becomes

$$\left|\frac{\Delta N_e}{N_{e0}}\right| = \left|\frac{U\sin 2(\theta+I)}{2V_{ph}}\right|. \tag{A.3}$$

Note that $|\Delta N_e| = 0$ when $\theta + I = 90°$, that is, when **k** is perpendicular to the geomagnetic field.

The neutral atmospheric density perturbation (ΔN) from its unperturbed value (N_0) is given by (Hines, 1960)

$$|\Delta N| \simeq \frac{N_0 U_x(\gamma-1)^{1/2}}{C}, \tag{A.4}$$

where C is the speed of sound and γ is the ratio of specific heats (= 1.4). Eqs. (A.3) and (A.4) together with the relation $\theta-\phi = \pm 90°$ gives

$$\frac{|\Delta N_e/N_{e0}|}{|\Delta N/N_0|} = \frac{0.8C\sin 2(\theta+I)}{V_{ph}\sin\theta}. \tag{A.5}$$

The dip angle I at Shigaraki is about 45° that results in

$$\frac{|\Delta N_e/N_{e0}|}{|\Delta N/N_0|} = \frac{0.8C\cos 2\theta}{V_{ph}\sin\theta}. \tag{A.6}$$

Since C at altitudes of 200–300 km is about 600 m s^{-1} and V_{ph} in our case is 100 m s^{-1}, Eq. (A.6) becomes

$$\frac{|\Delta N_e/N_{e0}|}{|\Delta N/N_0|} = \frac{4.8\cos 2\theta}{\sin\theta} \equiv X. \tag{A.7}$$

For southward/downward-propagating gravity waves ($0° \le \theta \le 90°$), $X \le 1$ for $41° \le \theta \le 50°$ (i.e., **k** is nearly perpendicular to the geomagnetic field): in this case $|\Delta N_e/\Delta N_{e0}|$ is largely suppressed (see Eq. (A.3)). $X \ge 1$ for other θ's.

References

Balan, N. and G. J. Bailey, Equatorial plasma fountain and its effects: Possibility of an additional layer, *J. Geophys. Res.*, **100**, 21,421–21,432, 1995.

Balan, N., Y. Otsuka, T. Tsugawa, S. Miyazaki, T. Ogawa, and K. Shiokawa, Plasmaspheric electron content in the GPS ray paths over Japan, *Earth Planets Space*, **54**, this issue, 71–79, 2002.

Brown, W. E. and W. R. Steiger, 6300 Å quantum efficiency of the recombination mechanism in the night-time *F* layer, *Planet. Space Sci.*, **20**, 11–24, 1972.

Evans, J. V., J. M. Holt, and R. H. Wand, A differential-Doppler study of traveling ionospheric disturbances from Millstone Hill, *Radio Sci.*, **18**, 435–451, 1983.

Garcia, F. J., M. J. Taylor, and M. C. Kelley, Two-dimensional spectral analysis of mesospheric airglow image data, *Appl. Opt.*, **36**, 7374–7385, 1997.

Hedin, A. E., MSIS-86 thermospheric model, *J. Geophys. Res.*, **92**, 4649–4642, 1987.

Hedin, A. E., M. A. Biondi, R. G. Burnside, G. Hernandez, R. M. Johnson, T. L. Killeen, C. Mazaudier, J. W. Meriwether, J. E. Salah, R. J. Sica, R. W. Smith, N. W. Spencer, V. B. Wickwar, and T. S. Virdi, Revised global model of thermospheric winds using satellite and ground-based observations, *J. Geophys. Res.*, **96**, 7657–7688, 1991.

Hines, C. O., Internal atmospheric gravity waves at ionospheric heights, *Can. J. Phys.*, **38**, 1441–1481, 1960.

Hocke, K. and K. Schlegel, A review of atmospheric gravity waves and traveling ionospheric disturbances: 1982–1995, *Ann. Geophysicae*, **14**, 917–940, 1996.

Hooke, W. H., Ionospheric irregularities produced by internal atmospheric gravity waves, *J. Atmos. Terr. Phys.*, **30**, 795–823, 1968.

Hooke, W. H., The ionospheric response to internal gravity waves. 1. The *F*2 region response, *J. Geophys. Res.*, **75**, 5535–5544, 1970.

Hunsucker, R. D., Atmospheric gravity waves generated in the high-latitude ionosphere: A review, *Rev. Geophys. Space Phys.*, **20**, 293–315, 1982.

Kubota, M., K. Shiokawa, M. K. Ejiri, Y. Otsuka, T. Ogawa, T. Sakanoi, H. Fukunishi, M. Yamamoto, S. Fukao, and A. Saito, Traveling ionospheric disturbances observed in the OI 630-nm nightglow images over Japan by using a multi-point imager network during the FRONT campaign, *Geophys. Res. Lett.*, **27**, 4037–4040, 2000.

Maeda, S. and S. Handa, Transmission of large-scale TIDs in the ionospheric *F*2–region, *J. Atmos. Terr. Phys.*, **42**, 853–859, 1980.

Ogawa, T., K. Ohtaka, T. Takami, Y. Yamamoto, M. Yamamoto, and S. Fukao, Medium- and large-scale TIDs simultaneously observed by NNSS satellites and the MU radar, in *Low-Latitude Ionospheric Physics*, (COSPAR Colloquia Series Vol. 7), edited by F. S. Kuo, 167 pp., Elsevier Science, Oxford, 1994.

Oliver, W. L., S. Fukao, M. Sato, Y. Otsuka, T. Takami, and T. Tsuda, Middle and upper atmosphere radar observations of the dispersion relation for ionospheric gravity waves, *J. Geophys. Res.*, **100**, 23,763–23,768, 1995.

Otsuka, Y., T. Ogawa, A. Saito, T. Tsugawa, S. Fukao, and S. Miyazaki, A new technique for mapping of total electron content using GPS network in Japan, *Earth Planets Space*, **54**, this issue, 63–70, 2002.

Porter, H. S. and T. F. Tuan, On the behavior of the *F*-layer under the influence of gravity waves, *J. Atmos. Terr. Phys.*, **36**, 135–157, 1974.

Porter, H. S., S. M. Silverman, and T. F. Tuan, On the behavior of airglow under the influence of gravity waves, *J. Geophys. Res.*, **79**, 3827–3833, 1974.

Saito, A., S. Fukao, and S. Miyazaki, High resolution mapping of TEC perturbations with the GSI GPS network over Japan, *Geophys. Res. Lett.*, **25**, 3079–3082, 1998.

Saito, A., M. Nishimura, M. Yamamoto, S. Fukao, M. Kubota, K. Shiokawa, Y. Otsuka, T. Tsugawa, T. Ogawa, M. Ishii, T. Sakanoi, and S. Miyazaki, Traveling ionospheric disturbances detected in the FRONT campaign, *Geophys. Res. Lett.*, **28**, 689–692, 2001.

Saito, A., M. Nishimura, M. Yamamoto, S. Fukao, T. Tsugawa, Y. Otsuka, S. Miyazaki, and M. C. Kelley, Observations of traveling ionospheric disturbances and 3-m scale irregularities in the nighttime *F*-region ionosphere with the MU radar and a GPS network, *Earth Planets Space*, **54**, this issue, 31–44, 2002.

Shibata, T. and T. Okuzawa, Horizontal velocity dispersion of medium-scale travelling ionospheric disturbances in the *F*-region, *J. Atmos. Terr. Phys.*, **45**, 149–159, 1983.

Shiokawa, K., Y. Katoh, M. Sato, M. K. Ejiri, T. Ogawa, T. Nakamura, T. Tsuda, and R. H. Wines, Development of optical mesosphere thermosphere imagers (OMTI), *Earth Planets Space*, **51**, 887–896, 1999.

Shiokawa, K., Y. Katoh, M. Satoh, M. K. Ejiri, and T. Ogawa, Integrating-sphere calibration of all-sky cameras for nightglow measurements, *Adv. Space Res.*, **26**, 1025–1028, 2000a.

Shiokawa, K., Y. Otsuka, T. Ogawa, K. Igarashi, S. Miyazaki, F. J. Rich, A. Saito, and K. Yumoto, Comprehensive imaging observations of midlatitude ionospheric disturbances during storm time substorms, *J. Geophys. Res.*, **105**, 27,067–27,080, 2000b.

Sobral, J. H. A., H. Takahashi, M. A. Abdu, P. Muralikrishna, Y. Sahai, C. J. Zamlutti, E. R. de Paula, and P. P. Batista, Determination of the quenching rate of the $O(^1D)$ by $O(^3D)$ from rocket-borne optical (630 nm) and electron density data, *J. Geophys. Res.*, **98**, 7791–7798, 1993.

Thome, G. D., Incoherent scatter observations of traveling ionospheric disturbances, *J. Geophys. Res.*, **69**, 4047–4049, 1964.

T. Ogawa (e-mail: ogawa@stelab.nagoya-u.ac.jp), N. Balan, Y. Otsuka, K. Shiokawa, C. Ihara, T. Shimomai, and A. Saito